Journal of Non-Newtonian Fluid Mechanics 265 (2019) 66–78

Contents lists available at ScienceDirect

Journal of Non-Newtonian Fluid Mechanics

journal homepage: www.elsevier.com/locate/jnnfm

A three-dimensional numerical study on the dynamics and deformation of a bubble rising in a hybrid Carreau and FENE-CR modeled polymeric liquid

Mitsuhiro Ohta[a,*], Tomohiro Furukawa[b], Yutaka Yoshida[b], Mark Sussman[c]

[a] Department of Mechanical Science, Graduate School of Technology, Industrial and Social Sciences, Tokushima University, 2-1 Minamijyousanjima-cho, Tokushima 770-8506, Japan
[b] Division of Applied Sciences, Graduate School of Engineering, Muroran Institute of Technology, 27-1 Mizumoto-cho, Muroran, Hokkaido 050-8585, Japan
[c] Department of Mathematics, Florida State University, Tallahassee, FL 32306, USA

ARTICLE INFO

Keywords:
Bubble rise motion
Viscoelastic property
Shear-thinning property
Hybrid non-Newtonian model
Multiphase flow

ABSTRACT

New results are reported on the simulation of the rise of a deforming gas bubble surrounded by a liquid exhibiting a blend of shear-thinning and viscoelastic properties. A new hybrid model has been developed which combines the Carreau model for emulating the shear-thinning property of the liquid with the Chilcott–Rallison (FENE-CR) model for treating the viscoelastic property of the liquid. The new hybrid model allows one to independently prescribe the shear-thinning and viscoelastic properties (parameters) to be used in a simulation. Computations are implemented using the coupled level-set and volume-of-fluid (CLSVOF) method for tracking the deforming gas-liquid interface. The interfacial jump conditions are enforced with the sharp interface approach. In this study, four parameters, the Eötvös number, Carreau model parameter for slope of decreasing viscosity, Deborah number, and viscoelastic polymer dumbbell length parameter, are varied in order to gain understanding for gas bubble morphology in liquids exhibiting both shear-thinning and viscoelastic properties. It is found that the extent of bubble deformation and the liquid stress field are strongly dependent on these 4 parameters with minimal correlation between the shear-thinning and viscoelastic parameters. The ability to vary shear-thinning and viscoelastic parameters independently of one another in the new hybrid Carreau and FENE-CR model enables one to conveniently predict gas bubble behavior in complex liquid polymers by parameterizing the new model from basic measurements of the polymers.

1. Introduction

For this article, we present a new hybrid Carreau [1] and Chilcott–Rallison (FENE-CR) [2] non-Newtonian model which we use in order to simulate the rise of a gas bubble in non-Newtonian liquids which possess both shear-thinning and viscoelastic properties. Our new hybrid shear-thinning and viscoelastic model allows one to directly make use of Carreau model parameters that are more accessible via experimental measurements than the parameters needed by existing viscoelastic shear-thinning models. In this paper, we demonstrate the versatility in being able to independently tune shear-thinning and viscoelastic properties of the non-Newtonian liquid. It is found that bubble morphology intimately depends on both the shear-thinning and viscoelastic properties. A striking example of the unique gas bubble morphology that our new model can predict is shown in Fig. 7. The shear-thinning property of the liquid transforms what would have been an oblate bubble with flat bottom into a cap bubble. The additional effect of the viscoelastic property for the liquid further superimposes a cusp onto the cap bubble. We are not aware of any researcher computationally reproducing a "cusped cap bubble." We remark that such a "cusped cap bubble" does exist in nature, as revealed experimentally in Fig. 5 of the article by Astarita and Apuzzo [3].

The dynamic motion of gas bubbles rising in non-Newtonian liquids is an object of interest in the fields of Chemical and Biochemical Engineering. The following experimental studies report on gas bubble rise motion in viscoelastic liquids; see [3–17]. Accompanying Computational Fluid Dynamics (CFD) simulations are beneficial for understanding otherwise hidden detailed flow structures and mechanisms governing the dynamic motion of gas bubbles rising in non-Newtonian liquids. This is because, with a numerical simulation, one can directly reveal the state of non-Newtonian properties such as the magnitude of the configuration tensor and the viscosity profile around a rising gas bubble. Starting with the innovative work of Noh et al. [18] on the numerical simulation of single gas bubbles rising in a viscoelastic liquid, a number of ensuing CFD studies for gas bubbles rising in non-Newtonian liquids have been presented; see [19–28]. We note that complementary numerical simulations on drop rise motion in a viscoelastic liquid have been presented by You et al. [29] and Ohta et al. [30].

* Corresponding author.
E-mail address: m-ohta@tokushima-u.ac.jp (M. Ohta).

https://doi.org/10.1016/j.jnnfm.2018.12.012
Received 8 June 2018; Received in revised form 25 December 2018; Accepted 29 December 2018
Available online 30 December 2018

Table 1
Chronological listing of methods for bubble and drop dynamics in Non-Newtonian liquids. Legend: (B)ubble, (D)rop, (L)attice (B)oltzmann, (L)evel (S)et, (V)olume (O)f (F)luid, (B)oundary (I)ntegral, (B)oundary (F)itted, (C)oupled (L)evel (S)et and (V)olume (O)f (F)luid, (B)oundary (E)lement, (A)ugmented (L)agrangian.

Reference	(B) or (D)?	Non-Newtonian model	Num. method	Rheological properties	Large deform?
[18]	(B)	FENE-CR	BF	Viscoelastic	No
[19]	(B), (D)	Maxwell	LB	Viscoelastic	No
[20]	(B)	Oldroyd-B	LS	Viscoelastic	Yes
[31]	(D)	Carreau–Yasuda	VOF	Shear-thinning	No
[32]	(D)	Carreau–Yasuda	VOF	Shear-thinning	Yes
[21]	(B)	Maxwell	LB	Viscoelastic	No
[22]	(B)	FENE-CR	BI	Viscoelastic	No
[23]	(B)	Oldroyd-B	LS	Viscoelastic	No
[24]	(B)	FENE-CR	CLSVOF	Viscoelastic	Yes
[29]	(D)	FENE-CR	BF	Viscoelastic	No
[33]	(B)	Papanastasiou	Elliptic grid generate	Inelastic viscoplastic	Yes
[25]	(B)	FENE-CR	BF	Viscoelastic	No
[30]	(D)	FENE-CR	CLSVOF	Viscoelastic	Yes
[26]	(B)	Maxwell	BE	Viscoelastic	Yes
[34]	(B)	Carreau	CLSVOF	Shear-thinning	Yes
[35]	(B)	Carreau	LS	Shear-thinning	Yes
[36]	(B)	Carreau	CLSVOF	Shear-thickening	Yes
[37]	(B)	Herschel–Bulkley	AL	Viscoplastic	Yes
[38]	(B)	Bingham	VOF	Viscoplastic	Yes
[27]	(B)	PTT	Elliptic grid generate	Viscoelastic shear-thinning	No
[39]	(B)	Carreau	VOF	Shear-thinning	Yes
[40]	(B)	Carreau	VOF	Shear-thinning	Yes
[28]	(B)	Carreau	VOF	Shear-thinning	Yes

In Table 1, we summarize previous work on the numerical simulation of bubbles/drops rising in non-Newtonian liquids. The combination of robustness and generality of our hybrid model distinguishes our present work from previous research. In many of the computational studies listed in Table 1, the Oldroyd-B model [41] or the FENE-CR model were adopted for modeling the viscoelastic liquids. The studies based on the Oldroyd-B or FENE-CR model are successful in explaining the effect of elasticity on a rising bubble or drop. For example, these studies report results illustrating the characteristic cusp-like trailing edge for a gas bubble rising through a viscoelastic liquid. However, discoveries obtained using the Oldroyd-B or FENE-CR model can be only applicable for the bubble rise motion in a viscoelastic liquid with a constant viscosity (so-called the Boger fluid [42]), because the shear-rate dependence of viscosity cannot be rendered in the Oldroyd-B or FENE-CR model.

Generally, most practical viscoelastic liquids, e.g. polymeric liquids, inherently possess both shear-thinning and viscoelastic properties. Accordingly, the Phan-Thien-Tanner (PTT) [43], FENE-P model [44,45], and Giesekus [46] models have been developed in order to take into account not only the viscoelastic property, but the shear-thinning property as well. However, these models have a downside in that one cannot easily isolate and control all of the essential shear-thinning properties using these models.

The Carreau, or Carreau–Yasuda [47] models, while not possessing a viscoelastic component, are more versatile models than the PTT, FENE-P, or Giesekus models at modeling all of the essential shear-thinning properties. The Carreau or Carreau–Yasuda models are designed so that the tunable parameters directly correspond to the essential and measurable shear-thinning properties (see Eq. (12)): (a) the exponent for viscosity power-law decay n, and (b) the shear-rate drop off parameter α. The power-law decay exponent n and shear rate drop off parameter α are readily available from measured rheological data. The tunable model parameters available for the PTT, FENE-P, or Giesekus models, are not flexible enough to tune all of the essential shear-thinning properties. For example, with the FENE-P model, the power law decay parameter n is always about 2/3 regardless of the FENE-P parameters chosen. The fact that the Carreau model parameters, by design, are more accessible through experimental measurements than the PTT, FENE-P or Giesekus models, motivates our development of the hybrid Carreau and FENE-CR model. Our new hybrid model allows one to easily consider the effects of both shear-thinning and viscoelastic properties of a given liquid surrounding vapor on determining bubble dynamics (i.e. bubble trajectory, speed, and boundary deformation).

Remark 1. In this article, we hybridize the Carreau shear-thinning model with the FENE-CR viscoelastic model (a Boger model). It could be that one can hybridize viscoelastic models other than the FENE-CR model with the Carreau shear-thinning model, as long as the viscoelastic model is a Boger model. In other words, a necessary criteria for hybridization is that the viscoelastic part must not have any implicitly built in shear-thinning properties. As a specific example of why hybridizing with a non-Boger model would be problematic, we refer to the following two articles, [44,45], which give a thorough analysis of the differences between the FENE-CR model in dimensionless form (a Boger model),

$$\frac{\partial \mathbf{A}}{\partial t} + \mathbf{u}\cdot\nabla\mathbf{A} = \mathbf{A}\cdot\nabla\mathbf{u} + (\nabla\mathbf{u})^{\mathrm{T}}\cdot\mathbf{A} - \frac{1}{1-\mathrm{Tr}(\mathbf{A})/b}(\mathbf{A}-\mathbf{I}), \tag{1}$$

and the FENE-P model in dimensionless form (a non-Boger model),

$$\frac{\partial \mathbf{A}}{\partial t} + \mathbf{u}\cdot\nabla\mathbf{A} = \mathbf{A}\cdot\nabla\mathbf{u} + (\nabla\mathbf{u})^{\mathrm{T}}\cdot\mathbf{A} - \frac{1}{1-\mathrm{Tr}(\mathbf{A})/b}\mathbf{A} + \mathbf{I}. \tag{2}$$

In these equations, $\mathbf{u}$ is the velocity vector, t is time, $\mathbf{A}$ is the polymer conformation tensor, b is the extensibility parameter. In Fig. 3 of [45], it is shown that under a simple shear flow, the viscosity for the FENE-CR method is constant as a function of the shear magnitude but for the FENE-P method, the viscosity decreases according to a power law model with the power being approximately 2/3. In Table 1 (for the FENE method) of Herrchen and Öttinger [45] and Fig. 1 (for the FENE-P method) of [44] it is shown that the two-thirds shear-thinning power law for the FENE-P and FENE models has little dependence on the extensibility parameter b. If one were to hybridize FENE-P with Carreau, there would be no way to prescribe a power-law that is lower than two-thirds for such a model. At the same time, it is known that many materials exist in nature which exhibit shear-thinning power-law rules for the viscosity that range less than one.

Remark 2. Relating to the previous remark, another possibly compatible viscoelastic model that can be hybridized with the Carreau shear-thinning model is the Oldroyd-B model (a Boger model). Our rationale

for choosing the FENE-CR model over Oldroyd-B is that the FENE-CR model requires no stabilization logic, such as the log-conformation approach [48], in order to prevent singularity formation in the configuration tensor ($\mathbf{A}$). In the FENE-CR model, the relaxation time is automatically reduced in order to prevent the uncontrollable growth for Tr($\mathbf{A}$).

2. Numerical analysis

2.1. Governing equations with the FENE-CR model and the multiphase flow projection method

In our study, the two-phase fluid flow is composed of air and a non-Newtonian liquid. The Navier–Stokes equations for non-Newtonian two-phase flow are numerically integrated in time using the projection method on Eulerian, block structured rectangular grids [24,49,50]. The deforming gas-liquid interface motion is approximated using the coupled level-set and volume-of-fluid (CLSVOF) method [51,52]. The CLSVOF method is a combination of the Volume-of-Fluid (VOF) method [53,54] and the level-set (LS) method [55]. In the VOF method, the VOF function F is defined as the volume fraction of the tagged fluid within a computational cell. The VOF function satisfies $F = 1$ for computational cells consisting of only the non-Newtonian liquid, $F = 0$ for computational cells consisting of only gas, and $0 < F < 1$ for a computational cell containing both gas and liquid. In the LS method, the LS function ϕ is defined to be a signed distance function: ϕ is positive in the non-Newtonian liquid, negative in the bubble, and the zero isosurface of ϕ represents the interface of the gas bubble. In the CLSVOF method, the LS function is maintained as the signed distance from the VOF reconstructed interface. The strategic coupling of the VOF function and the LS function enables one to accurately approximate the normal vector at any point on the interface while at the same time avoiding numerical loss of volume errors. Our numerical approach is stable and robust for a wide varying range of density and viscosity ratios.

A single set of governing equations describes the motion in both the gas bubble and the non-Newtonian liquid. Both the gas and liquid are assumed to behave as incompressible fluids. The viscoelastic property of the liquid is modeled via the FENE-CR model. We note that the polymer viscosity is zero in the bubble. The resulting Navier–Stokes equations for the non-Newtonian multiphase flow are:

$$\nabla \cdot \mathbf{u} = 0 \tag{3}$$

$$\frac{\partial \mathbf{u}}{\partial t} + (\mathbf{u}\cdot\nabla)\mathbf{u} = \frac{\mathbf{1}}{\boldsymbol{\rho}}\nabla\cdot\left[-p\mathbf{I} + 2\eta\boldsymbol{D} + \frac{\eta_P H f(\mathbf{A})}{\lambda}\mathbf{A}\right] - \frac{\boldsymbol{\sigma\kappa}}{\boldsymbol{\rho}}\nabla H + \mathbf{g} \tag{4}$$

Here, $\mathbf{u}$ is the velocity vector, t represents time, p is the pressure, $\mathbf{I}$ is the unit tensor, $\mathbf{D}$ is the rate of deformation tensor defined by $2\mathbf{D} = \nabla\mathbf{u} + (\nabla\mathbf{u})^{\mathrm{T}}$. ρ is the density, η is the viscosity, λ denotes a characteristic relaxation time. $\mathbf{A}$ is the polymer conformation tensor and represents an ensemble average of the dyadic product $\mathbf{RR}$ of the dumbbell end-to-end vector $\mathbf{R}$ (see Eq. (7)). κ is the curvature of the interface, H is the Heaviside function as a function of the LS function ϕ (see Eq. (6)) and $\mathbf{g}$ is the gravitational acceleration. The singular source term $\frac{\sigma\kappa}{\rho}\nabla H$ on the right hand side of the Navier–Stokes equation (Eq. (4)) is equivalent to specifying that the jump in the normal stress is $\sigma\kappa$.

Since we assume that both the gas and the suspending non-Newtonian liquid are incompressible and insoluble, the density ρ and viscosity η are taken to be constant within each respective fluid with a jump at the interface. The density and viscosity are expressed in terms of the Heaviside function,

$$\rho = \rho_L H + \rho_G(1-H), \eta = \eta_L H + \eta_G(1-H), \eta_L = \eta_S + \eta_P, \eta_P = c\eta_S. \tag{5}$$

The subscripts "G", "L", "S" and "P" denote gas, liquid, solvent and polymer respectively. c is a measure of the concentration of dumbbells (polymer). The Heaviside function, $H(\phi)$, is defined as follows:

$$H = \begin{cases} 1 & \phi \geq 0 \\ 0 & \phi < 0 \end{cases} \tag{6}$$

The time evolution of the polymer conformation tensor $\mathbf{A}$ is given by

$$\frac{\partial \mathbf{A}}{\partial t} + \mathbf{u}\cdot\nabla\mathbf{A} = \mathbf{A}\cdot\nabla\mathbf{u} + (\nabla\mathbf{u})^{\mathrm{T}}\cdot\mathbf{A} - \frac{f(\mathbf{A})}{\boldsymbol{\lambda}}(\mathbf{A}-\mathbf{I}). \tag{7}$$

In Eqs. (4) and (7), $f(\mathbf{A})$ is the spring force law of the individual dumbbells and specifies the nonlinear spring characteristics of the viscoelastic liquid. We prescribe the spring force law as follows:

$$f(\mathbf{A}) = \frac{1}{1 - \mathrm{Tr}(\mathbf{A})/L^2}. \tag{8}$$

L is the ratio of the length of a fully extended polymer dumbbell to its equilibrium length. The standard FENE-CR model liquid has a constant viscosity expressed by

$$\eta_L = \eta_S + \eta_P = \eta_S + c\eta_S = (1+c)\eta_S. \tag{9}$$

In the coupled level set and volume of fluid method (CLSVOF), the interface is represented by both the volume-of-fluid function F and the level set function ϕ; therefore both F and ϕ are advected by the velocity $\mathbf{u}$ of the flow field:

$$\frac{\partial F}{\partial t} + (\mathbf{u}\cdot\nabla)F = 0, \tag{10}$$

$$\frac{\partial \phi}{\partial t} + (\mathbf{u}\cdot\nabla)\phi = 0 \tag{11}$$

We give a summary of the steps of our numerical algorithm and the order of accuracy for each step. Since we discretize the advection, viscous, viscoelastic, and pressure gradient forces in separate steps (i.e. our method is an operator split method), the overall order of accuracy will be first order accurate. Each step of our method is discretized in a consistent and stable way, so that our overall method is guaranteed to converge as the grid is refined. This is what we observed in the present work (see Table 3 and also our previous work [50,52]).

1. Advance the interface by numerically integrating the volume of fluid equation (Eq. (10)) and the level set equation (Eq. (11)). (Second order algorithm [51]).
2. Numerically integrate the nonlinear advection terms that appear in Eq. (4). (Second order slope limited upwind algorithm [24,49,50,52]).
3. Numerically integrate the configuration tensor equation (Eq. (7)). (First order positivity preserving method is used [50]).
4. Numerically integrate the shear-thinning viscous and viscoelastic force terms using an explicit sub-cycling method [50].
5. Numerically integrate the surface tension and pressure gradient force terms (Projection method, see [24,49,50,52]).

2.2. Extension of the FENE-CR model to the hybrid Carreau and FENE-CR non-Newtonian model

Referring to Eq. (5), a Newtonian liquid corresponds to η_S equal to a constant and $\eta_P = 0$ ($c = 0$). A non-shear-thinning, FENE-CR non-Newtonian liquid corresponds to η_S equal to a constant and $\eta_P = c\eta_S$. An inelastic Carreau model liquid corresponds to,

$$\eta_L = \eta_\infty + (\eta_0 - \eta_\infty)\left[1 + (\alpha\cdot\dot{\gamma})^2\right]^{(n-1)/2}. \tag{12}$$

η_0 is the zero shear-rate viscosity, η_∞ is the infinite shear-rate viscosity, and n denotes the slope of decreasing viscosity. α is a model parameter representing the value of the shear-rate ($\dot{\gamma}$) for which the viscosity begins to drop off rapidly from η_0. $\dot{\gamma}$ can be evaluated by the second invariant of the rate-of-strain tensor:

$$\dot{\gamma} = \sqrt{2\mathbf{D} : \mathbf{D}} \tag{13}$$

We modify Eq. (9) in order to reflect the decreasing property of the viscosity of the polymer solution according to the Carreau model (Eq. (12)).

That is to say, the following form is incorporated into η_P, because η_P corresponds to the polymer contribution to the viscosity:

$$\eta_P = \eta_{P0}\left[1 + (\alpha \cdot \dot{\gamma})^2\right]^{(n-1)/2} \tag{14}$$

η_{P0} is the zero shear-rate viscosity of the polymer solution. Eq. (14) can be also written in the following form (Eq. (15)), since η_P is defined by $c\eta_S$:

$$\eta_P = \eta_{P0}\left[1 + (\alpha \cdot \dot{\gamma})^2\right]^{(n-1)/2} = c\eta_S = c_0\left[1 + (\alpha \cdot \dot{\gamma})^2\right]^{(n-1)/2}\eta_S \tag{15}$$

c_0 should be interpreted as the polymer concentration parameter in zero shear-rate regions. Finally, we obtain a new expression for η_L by substituting Eq. (14) into Eq. (9):

$$\eta_L = \eta_S + \eta_{P0}\left[1 + (\alpha \cdot \dot{\gamma})^2\right]^{(n-1)/2} \tag{16}$$

Another way to write Eq. (16) is to define a "total liquid constant viscosity,"

$$\eta_0 = \eta_S + \eta_{P0},$$

and rewrite η_L in terms of η_0:

$$\eta_L = \eta_S + (\eta_0 - \eta_S)\left[1 + (\alpha \cdot \dot{\gamma})^2\right]^{(n-1)/2}. \tag{17}$$

η_S is interpreted as the infinite shear-rate viscosity (η_∞) in the original Carreau model (Eq. (12)). Eq. (17) is identical with the original Carreau model (Eq. (12)) when, $\eta_S = \eta_\infty$.

3. Numerical grid, initial conditions, and physical properties

The numerical grid fills a 3d-rectangular box as shown in Fig. 1. The 3d-rectangular box has the $x \times y \times z$ dimensions of either $4d \times 4d \times 20d$ or $4d \times 4d \times 24d$ respectively. d is the diameter of a spherical bubble sharing the same volume as the bubble in our numerical simulations.

The height of $Z = 20d$ was used for the large-sized bubble ($Eo = 176$) simulations and $Z = 24d$ was employed for the other smaller bubble simulations ($Eo = 20$ and $Eo = 44$).

The size of the computational system was decided upon by determining the smallest domain in which the results would not be influenced by the domain walls; see Table 3.

A stationary spherical gas bubble was initially imposed at the bottom of the computational domain: the coordinate of the initial position of the bubble center was ($2d$, $2d$, $0.75d$). The initial velocity was set to zero in the entire computational domain. From $t = 0$, the gas bubble begins to freely rise due to gravity. Outflow boundary conditions were applied on all the walls of the domain box. Outflow boundary conditions for the polymer configuration tensor **A** corresponds to homogeneous Neumann conditions for all components of **A**.

For the purpose of saving computational resources, our numerical simulations were performed on an adaptive hierarchy of grids using the dynamic adaptive mesh refinement technique (AMR) [56]. The adaptive grids are dynamically adjusted based on the location of a deforming gas-liquid interface. Fig. 2 illustrates the AMR system. AMR enables one to increase the grid resolution in regions near the interface. The left side of Fig. 2 illustrates a schematic view of the hierarchical grid structure and the right side corresponds to an actual computational example for a gas bubble rising through a viscoelastic liquid. The mesh hierarchy is composed of different levels of refinement ranging from coarsest ($\ell = 0$, "Level-0") to finest ($\ell = \ell_{max}$, "Level-6"). The refinement ratio between levels is two: $\Delta x^{\ell+1} = 0.5\Delta x^{\ell}$. In this study, we used the AMR system with a maximum prescribed level of "Level-2" (as illustrated in Fig. 2). In our adaptive mesh refinement algorithm, velocity and the configuration tensor in coarse grid cells that neighbor fine grid cells are interpolated from the coarse grid using bilinear interpolation in order to initialize "ghost" fine cells. The bilinear interpolation procedure produces interpolated fine grid data as a linear combination

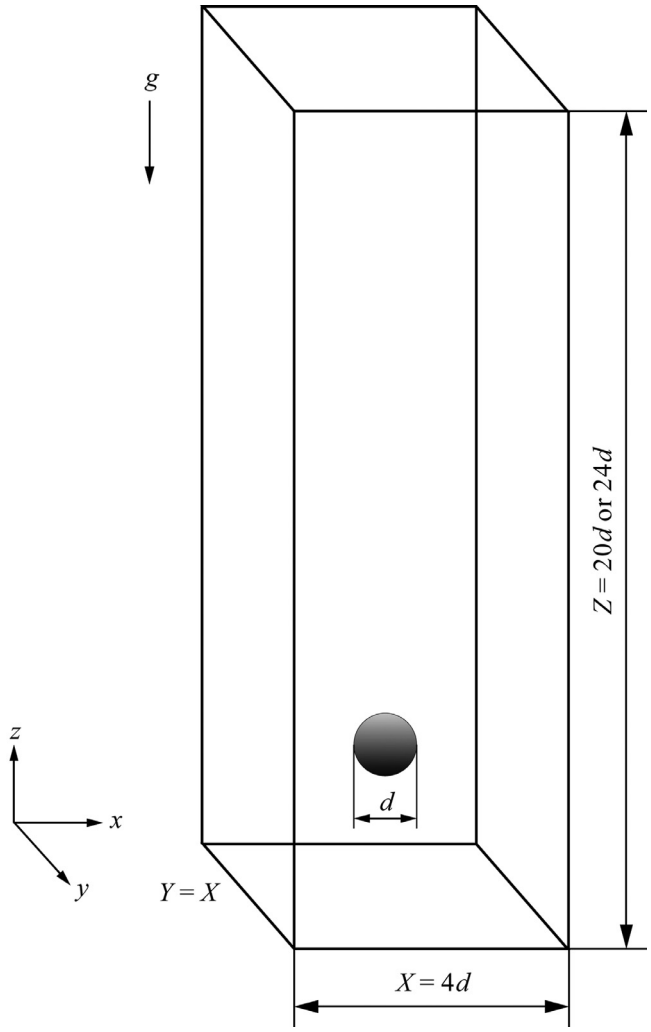

Fig. 1. Computational system.

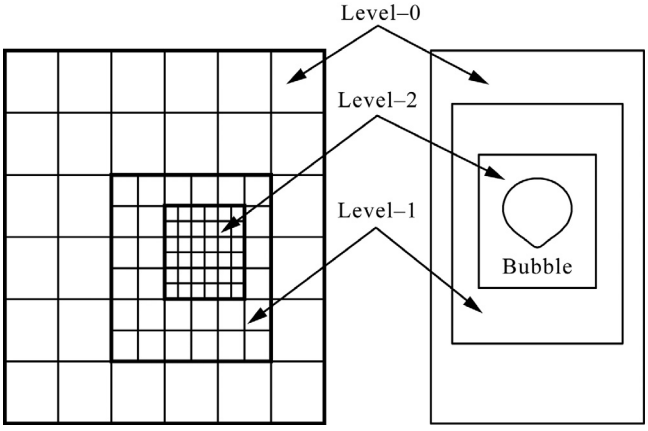

Fig. 2. Grid structure using the adaptive mesh refinement system.

of the coarse grid data. The interpolation coefficients are all positive and restricted to a number between 0 and 1. This property of the interpolation from coarse grid data to fine grid data guarantees that the polymer configuration tensor **A** is always positive definite symmetric [50].

The physical properties for our simulations of a bubble rising in a non-Newtonian liquid are defined in Table 2.

Table 2
Physical properties for a bubble rising in a shear-thinning viscoelastic liquid.

Symbol	Name	Definitions/Units	value(s)
M	Morton number	$g\eta_0^4(\rho_L-\rho_G)/(\rho_L^2\sigma^3)$	78
Eo	Eötvös number	$(\rho_L-\rho_G)gd^2/\sigma$	20, 44, 176
	Density ratio	ρ_G/ρ_L	1.2×10^{-3}
	Zero shear-rate viscosity ratio	η_G/η_0	1.8×10^{-5}
η_S	Solvent viscosity	Pa·s	1.0×10^{-3}
c_0	Polymer concentration parameter in η_0 regions		999
η_0	Zero shear-rate viscosity	Pa·s	1.0
α	Carreau model parameter	s	1.0
n	Carreau model parameter		0.5, 0.8
De	Deborah number	$\lambda/(d/V)$	1.0, 5.0
L	FENE-CR model parameter		2.5, 10.0

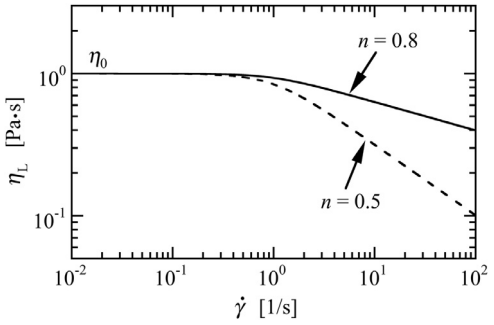

Fig. 3. Viscosity profile employed in this study.

Table 3
Grid refinement study and domain size sensitivity study: $Eo = 176$, $n = 0.5$, $L = 10.0$ and $De = 5.0$. The computed Reynolds number is $Re^{\text{comp}} = \frac{\rho_L V^{\text{comp}} d}{\eta_0}$. V^{comp} is the computed terminal bubble rise velocity.

Δx_{fine}	Domain dimensions	Computed Reynolds number Re^{comp}
$d/24$	$4d(X)\times4d(Y)\times20d(Z)$	9.5
$d/32$	$4d(X)\times4d(Y)\times20d(Z)$	9.6
$d/32$	$6d(X)\times6d(Y)\times20d(Z)$	9.6

Remarks:

- d corresponds to the effective diameter of a bubble. The values of $Eo = 20, 44, 176$ correspond to $d = 10, 15, 30$ mm, respectively.
- V corresponds to a characteristic terminal bubble rise velocity.
- The viscosity profiles that result from the Carreau parameters α and n in Table 2 are plotted in Fig. 3.
- In large Eo and small M conditions, it has been demonstrated in [57] that the terminal bubble rise motion was sensitive to the initial bubble conditions. In Table 2, we tested the values of $n = 0.5$ and $n = 0.8$. Our rationale for not reporting results for $n < 0.5$ is that if we decrease n to be below 0.5, the effective value of M, due to shear-thinning, becomes very small and there is a good possibility that the bubble rise motion is sensitive to the initial bubble condition. i.e. the results might not be repeatable.

A grid refinement and domain size sensitivity study was performed for a rising bubble corresponding to the following dimensionless parameter set: $Eo = 176$, $n = 0.5$, $L = 10.0$ and $De = 5.0$. We chose this parameter set because it corresponds to the severest combination of bubble deformation and strongest non-Newtonian effects. The results of our grid refinement and domain size sensitivity study are reported in Table 3 and Fig. 4.

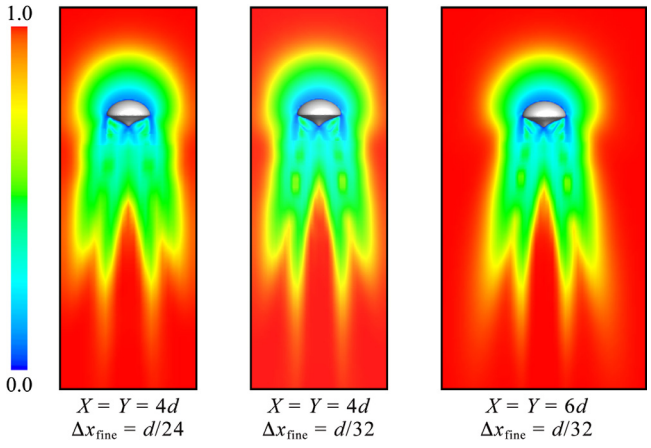

Fig. 4. Viscosity profile around the bubble depending on grid and domain sizes.

From the results reported in Table 3, we see that the computed values of Re^{comp} differ at most by two percent. Fig. 4 illustrates that there is no change in the non-Newtonian bubble morphological categorization as a result of grid refinement or enlargening of the domain size. After taking into account the results of our grid refinement study and domain size sensitivity study, we employed the computational system of, $\Delta x_{\text{fine}} = d/32$ and $4d(X)\times4d(Y)\times20d(Z)$, for the condition of $Eo = 176$ and employed the computational system of, $\Delta x_{\text{fine}} = d/24$ and $4d(X)\times4d(Y)\times24d(Z)$, for the conditions of $Eo = 20$ and $Eo = 44$. We note that the smaller Eötvös number conditions, $Eo = 20$ and $Eo = 44$, require a taller domain size of $Z = 24d$.

4. Results and discussion

4.1. Bubble shape

In Figs. 5 through 7, we show the terminal bubble shapes corresponding to different values of n, L, De and Eo. In Tables 4–6, we summarize the sensitivity of the terminal bubble shape due to whether the liquid is Newtonian, shear-thinning (i.e. purely viscous), viscoelastic, or hybrid shear-thinning and viscoelastic.

In Table 7, we summarize the effect of increasing the Eötvös number for a bubble rising in a (a) Newtonian liquid, (b) Carreau liquid, and (c) hybrid Carreau and FENE-CR model liquid. We point out that the case for $Eo = 176$ and the hybrid Carreau and FENE-CR model liquid exhibits a very distinctive hybrid cap and cusped bubble (see Fig. 5 of [3]). The shear-thinning property induces the cap shape rather than a oblate or prolate shape. The viscoelastic property induces a cusp at the base of the cap bubble.

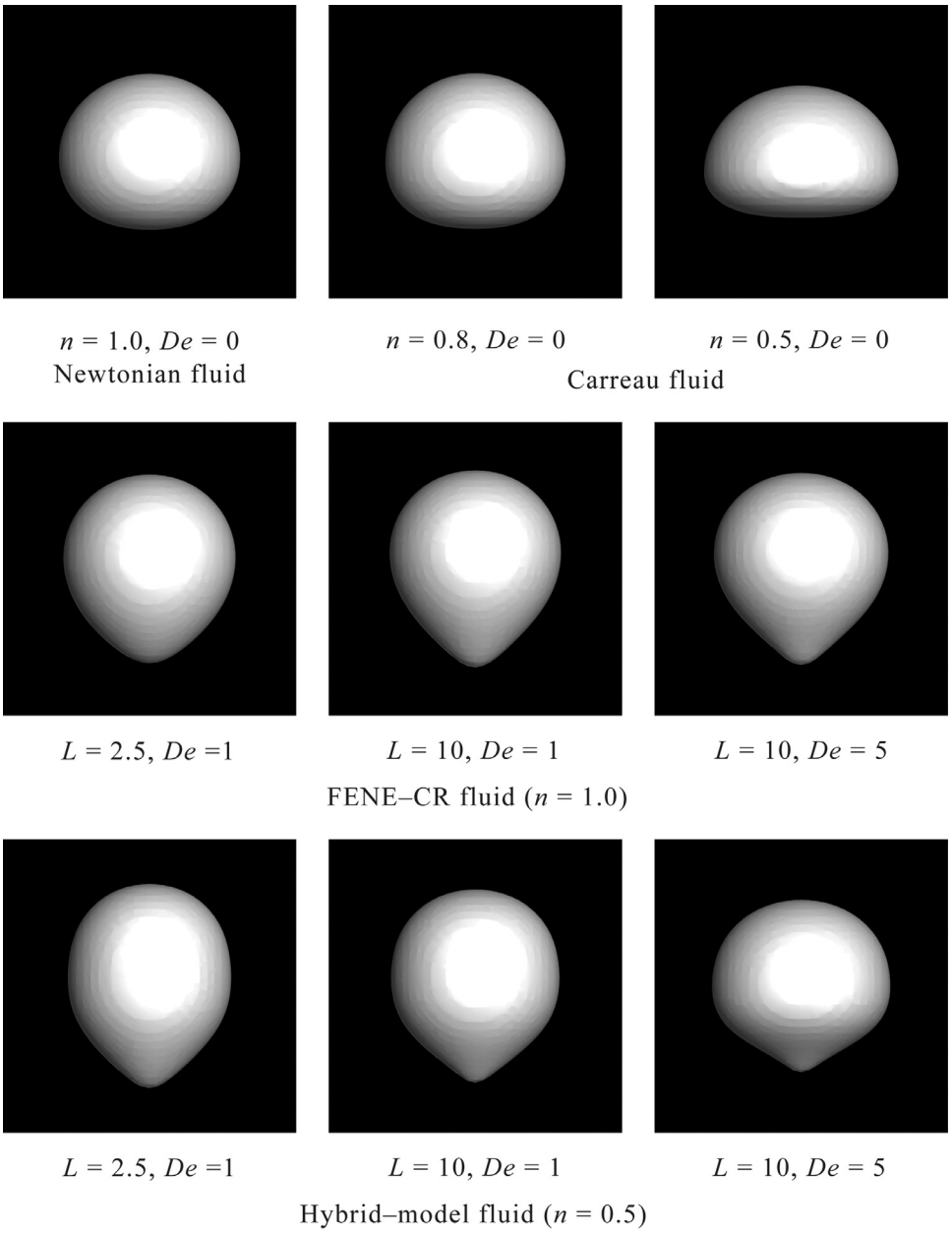

Fig. 5. Bubble shape depending on a variety of fluids for the condition of $Eo = 20$.

Table 4
Bubble morphology for a bubble rising in a (a) Newtonian or Carreau model liquid, (b) FENE-CR model liquid, and (c) Hybrid Carreau and FENE-CR model liquid for the condition of $Eo = 20$. The Hybrid model, due to the shear-thinning property, exhibits a more angular cusp shape than the corresponding FENE-CR cases. See Fig. 5.

Liquid constitutive model	Liquid 1	Liquid 2	Liquid 3
Newtonian or Carreau (a)	$n = 1.0$ (Newtonian) Slight deformation	$n = 0.8$ (Carreau) Slight deformation	$n = 0.5$ (Carreau) Oblate
FENE-CR (b)	$L = 2.5$, $De = 1$ Prolate, blunt cusp	$L = 10.0$, $De = 1$ Prolate, sharp cusp	$L = 10.0$, $De = 5$ Prolate, sharp cusp
Hybrid $n = 0.5$ (c)	$L = 2.5$, $De = 1$ Prolate, blunt cusp	$L = 10.0$, $De = 1$ Prolate, pinched cusp	$L = 10.0$, $De = 5$ Oblate, pinched cusp

Table 5
Bubble morphology for a bubble rising in a (a) Newtonian or Carreau model liquid, (b) FENE-CR model liquid, and (c) Hybrid Carreau and FENE-CR model liquid for the condition of $Eo = 44$. The rise speed is faster than the $Eo = 20$ case, resulting in a more significant reduction of viscosity for the shear-thinning or hybrid cases. The reduction in viscosity results in more pronounced deformation. See Fig. 6.

Liquid constitutive model	Liquid 1	Liquid 2	Liquid 3
Newtonian or Carreau (a)	$n = 1.0$ (Newtonian) Oblate, flat bottom	$n = 0.8$ (Carreau) Oblate, flat bottom	$n = 0.5$ (Carreau) Cap
FENE-CR (b)	$L = 2.5$, $De = 1$ Prolate, cusp	$L = 10.0$, $De = 1$ prolate, cusp	$L = 10.0$, $De = 5$ Prolate, cusp
Hybrid $n = 0.5$ (c)	$L = 2.5$, $De = 1$ Oblate, blunt cusp	$L = 10.0$, $De = 1$ Oblate, pinched cusp	$L = 10.0$, $De = 5$ Oblate, pinched cusp

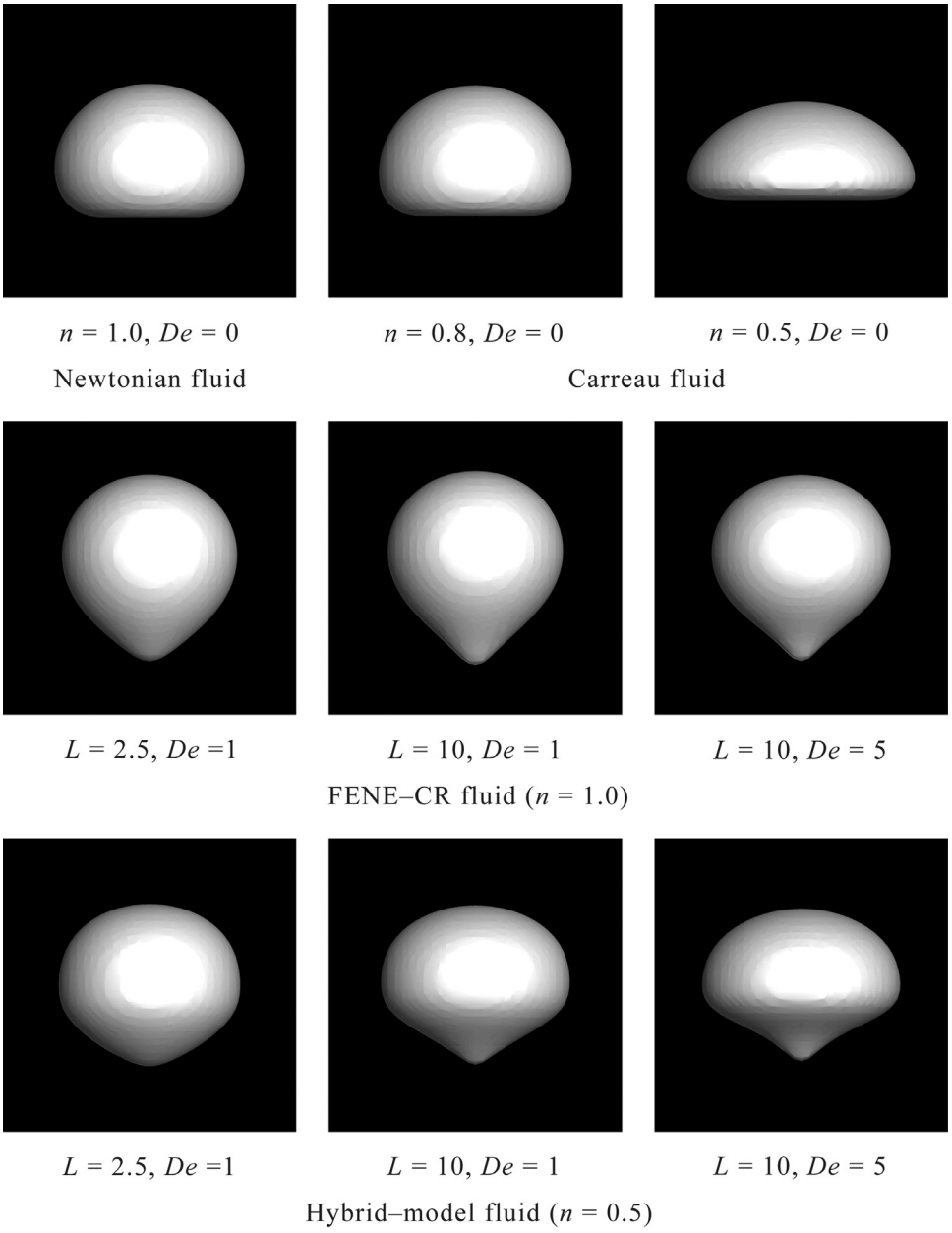

Fig. 6. Bubble shape depending on a variety of fluids for the condition of $Eo = 44$.

Table 6
Bubble morphology for a bubble rising in a (a) Newtonian or Carreau model liquid, (b) FENE-CR model liquid, and (c) Hybrid Carreau and FENE-CR model liquid for the condition of $Eo = 176$. The rise speed is even faster than the $Eo = 44$ case, resulting in the most significant reduction of viscosity for the shear-thinning or hybrid cases. The combination of the high Eötvös number, $Eo = 176$, and the shear-thinning viscosity will shift the bubble into the cap bubble regime. Furthermore, the viscoelastic property of a liquid results in a bubble shape that is both cap bubble and cusped. See Fig. 7.

Liquid constitutive model	Liquid 1	Liquid 2	Liquid 3
Newtonian or Carreau (a)	$n = 1.0$ (Newtonian) Oblate, flat bottom	$n = 0.8$ (Carreau) Cap	$n = 0.5$ (Carreau) Cap
FENE-CR (b)	$L = 2.5$, $De = 1$ Oblate	$L = 10.0$, $De = 1$ Oblate, cusp	$L = 10.0$, $De = 5$ Oblate, sharp cusp
Hybrid $n = 0.5$ (c)	$L = 2.5$, $De = 1$ Cap	$L = 10.0$, $De = 1$ Cap, mild cusp	$L = 10.0$, $De = 5$ Cap, sharp cusp

4.2. Shear-thinning viscosity effect

In Figs. 8 and 9, we show the viscosity profile that is generated by a gas bubble rising in either a Newtonian, shear-thinning, or hybrid shear-thinning and viscoelastic liquid. Fig. 8 reports the viscosity profile for the small bubble ($Eo = 20$) and Fig. 9 reports the viscosity profile for the large bubble ($Eo = 176$).

The value of the viscosity is normalized by η_0. The red area (= 1.0) corresponds to regions in the computational domain in which the local viscosity is η_0 and the dark blue area (≈ 0) corresponds to regions in the computational domain in which the local viscosity matches η_G. Note that the dark blue area of η_G is hidden by the bubble shape.

As expected, the viscosity around the bubble in the Newtonian liquid is constant, and the viscosity around the bubble is reduced for the

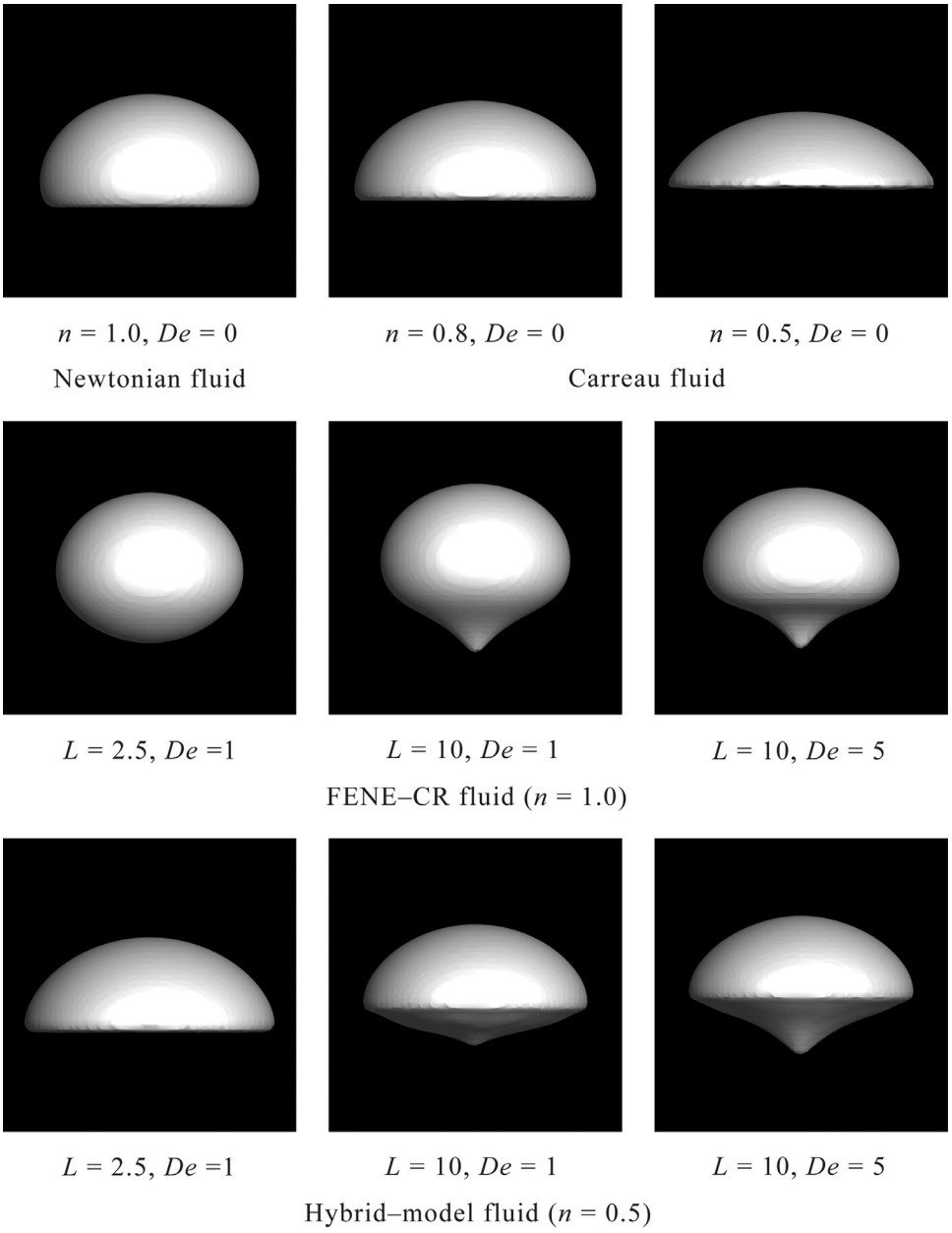

Fig. 7. Bubble shape depending on a variety of fluids for the condition of $Eo = 176$.

Table 7
Bubble morphology as the Eötvös number is increased for a bubble rising in a (a) Newtonian liquid, (b) Carreau model liquid, and (c) Hybrid Carreau and FENE-CR model liquid. The shear-thinning property of the liquid transforms what would have been an oblate bubble with flat bottom into a cap bubble. The addition of a viscoelastic property for the liquid further superimposes a cusp onto the cap bubble.

Eo	Newtonian $n = 1.0$	$n = 0.5$ (Carreau)	$n = 0.5$, $L = 10.0$, $De = 5$ (Hybrid)
20	Slight deformation	oblate	Oblate, pinched cusp
44	Oblate, flat bottom	Cap	Oblate, pinched cusp
176	Oblate, flat bottom	Cap	Cap, sharp cusp

other shear-thinning cases. Also as expected, a bubble rising in an $n = 0.5$ shear-thinning liquid will induce a larger reduction in the viscosity than the $n = 0.8$ case.

Remarks on Figs. 8 and 9:

- The regions of decreased viscosity for the shear-thinning or hybrid shear-thinning cases implicitly depend on the viscoelastic properties of the liquid since the terminal bubble shape is effected by the viscoelastic properties.
- There is a nonlinear feedback mechanism between the shear-thinning and viscoelastic properties and the resulting shape and rise speed of a bubble rising in a given non-Newtonian liquid. The shear-thinning and/or viscoelastic effects alter the shape and rise speed

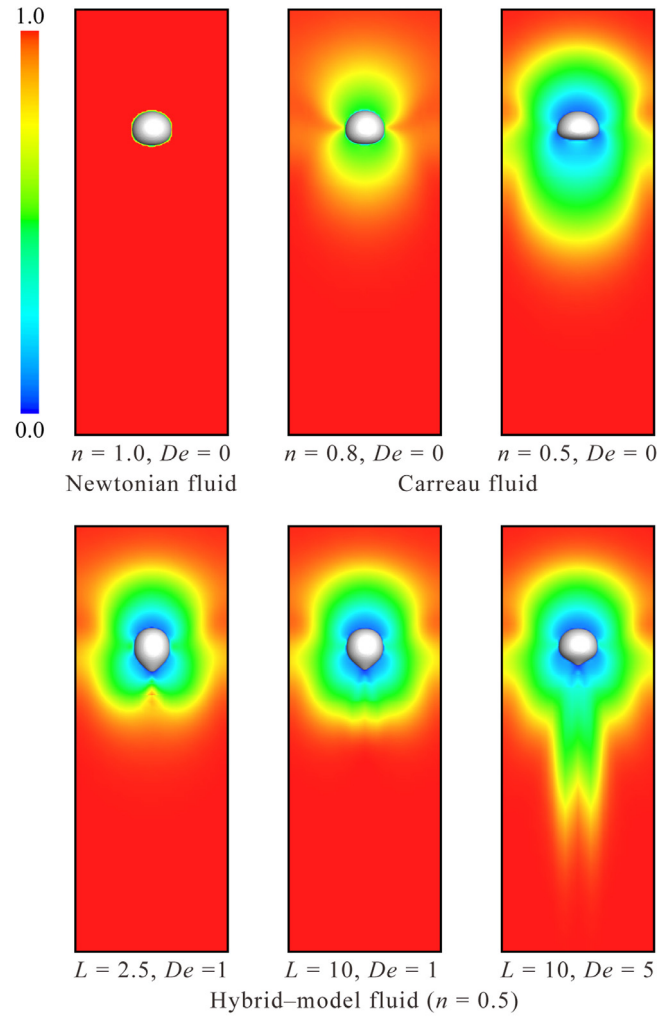

Fig. 8. Viscosity profile around the bubble depending on model fluids for the condition of $Eo = 20$.

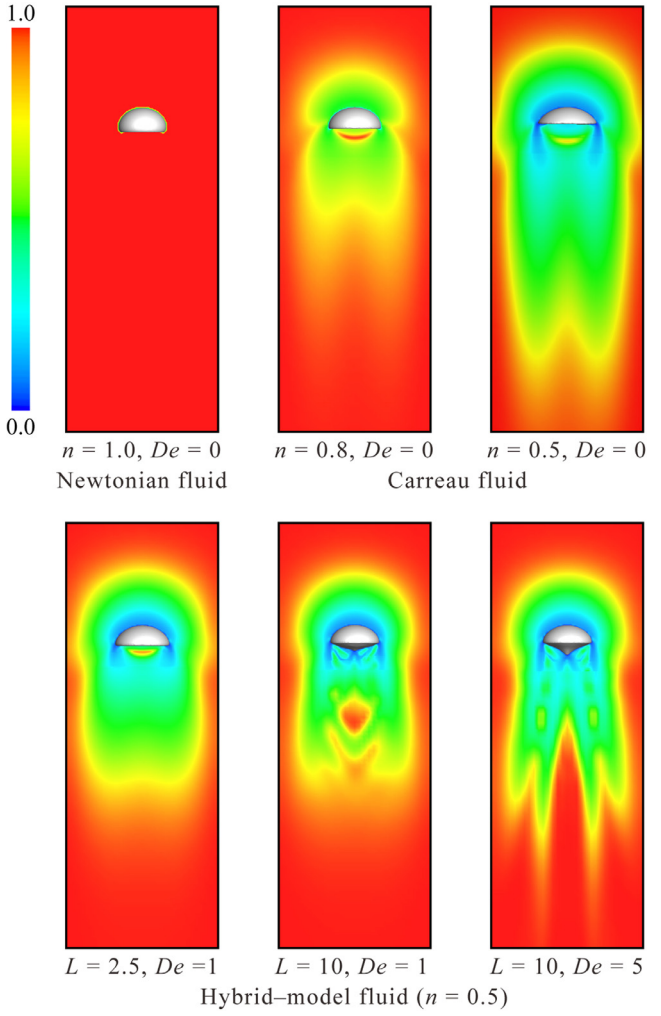

Fig. 9. Viscosity profile around the bubble depending on model fluids for the condition of $Eo = 176$.

of a rising bubble, which in turn alters the distribution of viscosity reduction, which again alters the shape.

- Increasing the Eötvös number results in a more substantial viscosity reduction further downstream of a rising bubble.

Fig. 10 shows the azimuthal viscosity profile around the bubble for the condition of $Eo = 176$ with $n = 0.5$, $L = 10$, and $De = 5$. In Fig. 10, the azimuthal viscosity profile is drawn at the constant z cross-sections A, B and C as indicated on the right side of Fig. 10. For the viscosity profiles corresponding to the cross-sections A and B, the viscosity is axisymmetric and radially increasing. This is expected since the shear rate near the bubble is larger, resulting in a smaller viscosity. The viscosity around the cusped part of the bubble at cross-section C is not axisymmetrically-distributed. Three-dimensional non-axisymmetric patterns appear at the cusped part behind the bubble.

4.3. Viscoelastic effect

In Fig. 11, we show the profile of the trace of the configuration tensor, Tr(**A**), for the cases of a bubble rising in a FENE-CR or hybrid Carreau and FENE-CR liquid.

The trace of **A** cannot fall below three ("blue" color) and can never exceed $L^2 = 100$.

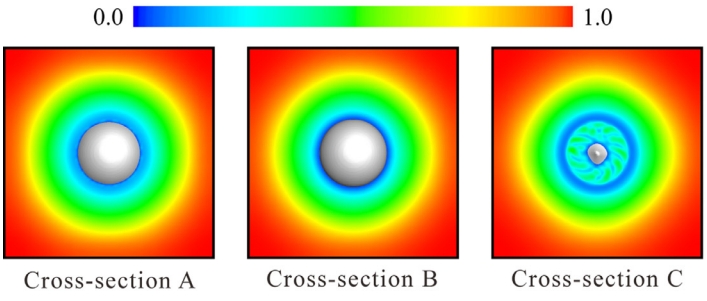

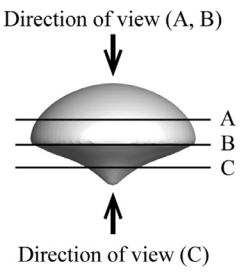

Fig. 10. Azimuthal viscosity profile around the bubble depending on cross-sections for the condition of $Eo = 176$ with $n = 0.5$, $L = 10$ and $De = 5$.

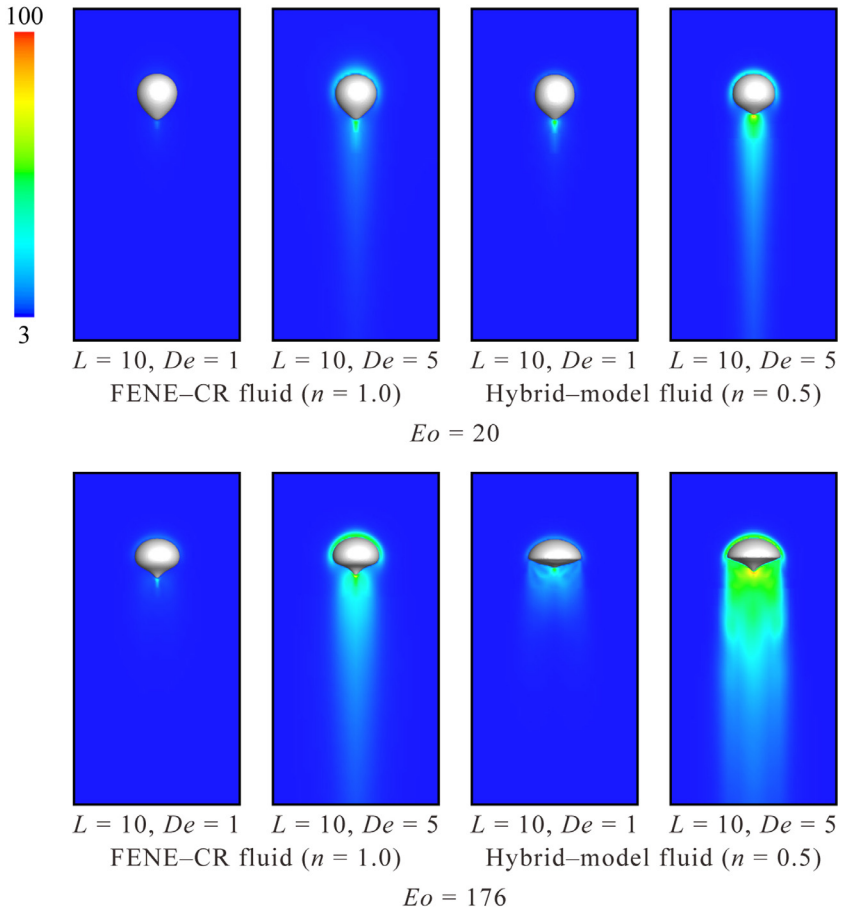

Fig. 11. Tr(**A**) profile around the bubble depending on model fluids. (For interpretation of the references to color in this figure legend, the reader is referred to the web version of this article.)

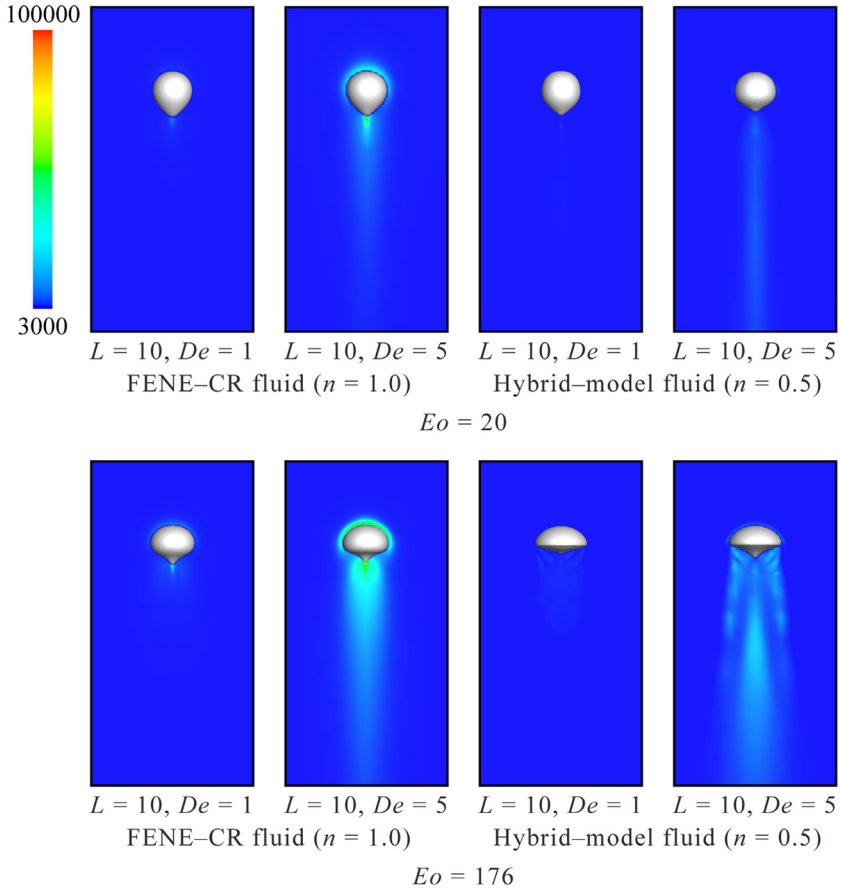

Fig. 12. [$c \times$ Tr(**A**)] profile around the bubble depending on model fluids.

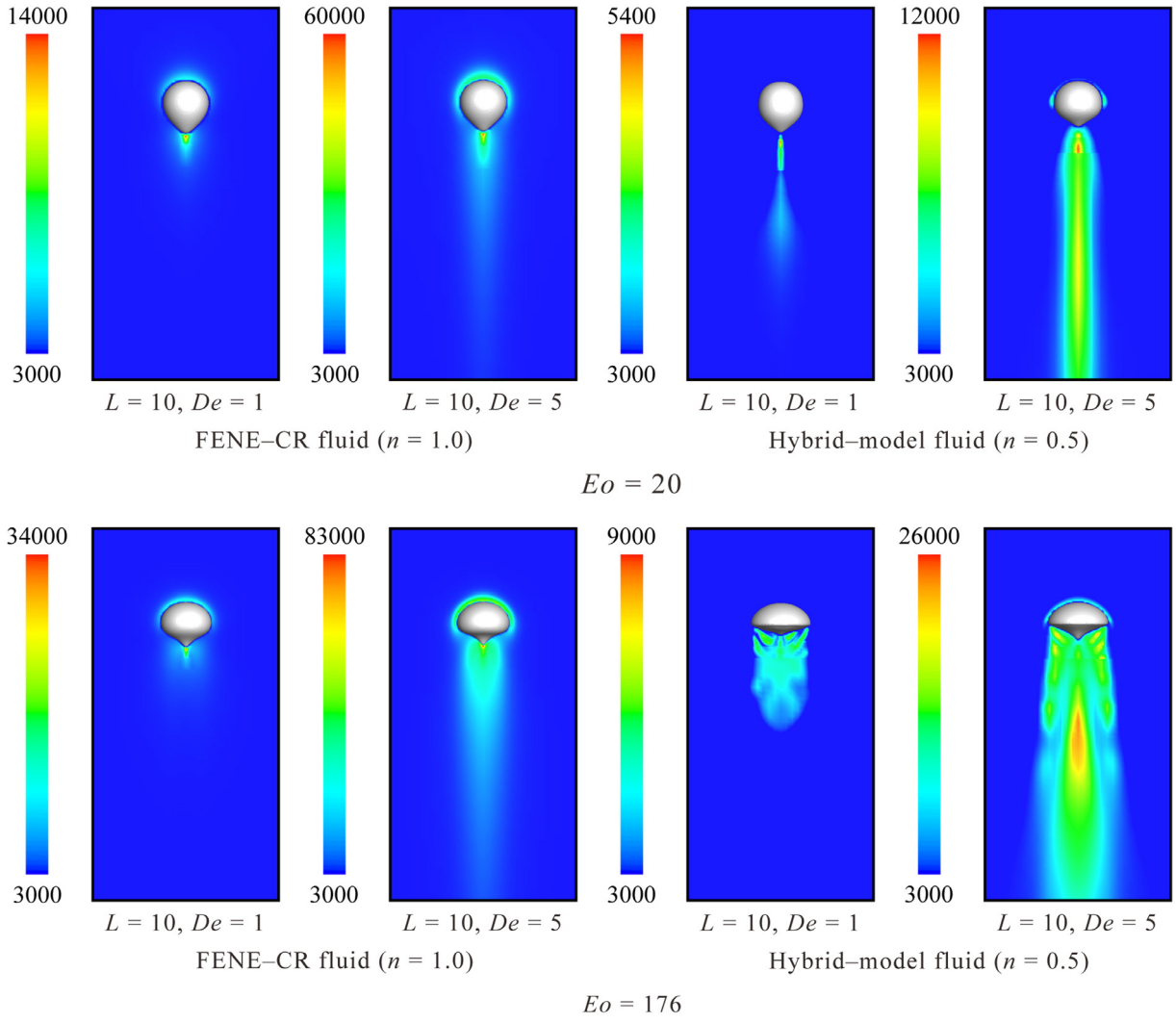

Fig. 13. $[c \times \mathrm{Tr}(\mathbf{A})]$ profile around the bubble depending on model fluids.

Remarks on Fig. 11:

- The magnitude of the viscoelastic forces, as measured by the trace of **A**, is always larger for the $Eo = 176$ cases than the $Eo = 20$ cases. This is because the oblate or cap shaped bubbles ($Eo = 176$) rise faster than the prolate shaped bubbles ($Eo = 20$). As a result of larger viscoelastic force, the $Eo = 176$ cases exhibit a sharper (more well defined) cusp.
- The case for a bubble rising in a hybrid shear-thinning and viscoelastic liquid with $Eo = 176$ exhibits the most effect from the viscoelastic property. We hypothesize that the shear-thinning property induces a cap shape, which rises the fastest of all the cases, thereby inducing the largest viscoelastic stresses.

4.4. Combined effect of shear-thinning and viscoelastic properties

In this section, we analyze the shear-thinning effect on the viscoelastic stress. In Figs. 12 and 13 we plot the contours of $[c \times \mathrm{Tr}(\mathbf{A})]$. Also we report $[c \times \mathrm{Tr}(\mathbf{A})]_{\max}$ in Table 8. We report $[c \times \mathrm{Tr}(\mathbf{A})]$ because it is an indicator of the magnitude of the viscoelastic stress for our hybrid model:

$$\eta_{\mathrm{P}}\mathbf{A} = c\eta_{\mathbf{S}}\mathbf{A} = \mathbf{c_0}\eta_{\mathrm{S}}\left[1 + (\alpha \cdot \dot{\gamma})^2\right]^{(n-1)/2}\mathbf{A}. \tag{18}$$

Referring to the Navier–Stokes equation, Eq. (4), the polymer contribution to the viscous stress is $2\eta_{\mathrm{P}}\mathbf{D}$ and the polymer contribution to the viscoelastic stress is $\eta_{\mathrm{P}} \times \mathbf{A}$. For the FENE-CR model, $\eta_{\mathbf{P}} = c\eta_{\mathbf{S}}$, is a constant. For our new hybrid model, η_{P} depends on $\dot{\gamma}$ as described in Eqs. (15) or (18).

Table 8
Dependence of $[c \times \mathrm{Tr}(\mathbf{A})]_{\max}$ on *L*, *De*, *n*, and *Eo* for a bubble rising in a FENE-CR model or hybrid Carreau and FENE-CR model liquid. As *Eo* is increased, then $[c \times \mathrm{Tr}(\mathbf{A})]_{\max}$ increases. This is because the terminal rise speed increases as *Eo* increases. Also, the values of $[c \times \mathrm{Tr}(\mathbf{A})]_{\max}$ are smaller for the hybrid model than the FENE-CR model (all other parameters being equal) since *c* decreases as $\dot{\gamma}$ increases for the hybrid model (*c* is fixed for the FENE-CR model).

Liquid constitutive model	*L*	*De*	*n*	*Eo*	$[c \times \mathrm{Tr}(\mathbf{A})]_{\max}$
FENE-CR	10	1	1.0	20	1.4×10^{4}
FENE-CR	10	5	1.0	20	5.9×10^{4}
Hybrid	10	1	0.5	20	5.4×10^{3}
Hybrid	10	5	0.5	20	1.1×10^{4}
FENE-CR	10	1	1.0	176	3.4×10^{4}
FENE-CR	10	5	1.0	176	8.2×10^{4}
Hybrid	10	1	0.5	176	9.0×10^{3}
Hybrid	10	5	0.5	176	2.5×10^{4}

In contrast to Fig. 11, Figs. 12 and 13 take into account the effect of the shear-thinning induced decrease in viscosity on the viscoelastic stress. We note that the distribution of $[c \times \mathrm{Tr}(\mathbf{A})]$ in Fig. 12 corresponding to the FENE-CR case is the same as the distribution of $[\mathrm{Tr}(\mathbf{A})]$

in Fig. 11 corresponding to the FENE-CR case except that the magnitudes for $[c \times \mathrm{Tr}(\mathbf{A})]$ will be approximately 1000 times larger since $c = c_0 = 999$.

On the other hand, the distribution of $[c \times \mathrm{Tr}(\mathbf{A})]$ corresponding to a bubble rising in the hybrid model liquid in Fig. 12 is quite different from the distribution of $\mathrm{Tr}(\mathbf{A})$ corresponding to the hybrid model liquid in Fig. 11. It is clear that the magnitude of the viscoelastic stresses in terms of $[c \times \mathrm{Tr}(\mathbf{A})]$ becomes very small compared to that for the FENE-CR model liquid. From these results for the hybrid model liquid, the importance of the influence of the shear-thinning effect on the viscoelastic stresses is revealed. It is also apparent from the hybrid results in Figs. 12 and 13 that strong viscoelastic stresses are not required in order to form the characteristic viscoelastic induced cusped shape at the base of a rising bubble. In Table 8, we compare $[c \times \mathrm{Tr}(\mathbf{A})]_{\max}$ for the FENE-CR cases versus the hybrid cases.

In order to better illustrate the results in Fig. 12 for $[c \times \mathrm{Tr}(\mathbf{A})]$, we plot Fig. 13 which is the same as Fig. 12 except that we focus on a more compact range of contours for $[c \times \mathrm{Tr}(\mathbf{A})]$ in order to better differentiate between the different contour levels. From Fig. 13, it can be observed that the $[c \times \mathrm{Tr}(\mathbf{A})]$ profile, about a rising bubble, is closely related to the surrounding liquids' viscosity profile. In the case of $Eo = 20$, the viscoelastic stresses for the condition of $L = 10$ and $De = 1$ act in very confined regions along the center line behind the bubble. At the same time, stronger viscoelastic-stress regions for the condition of $L = 10$ and $De = 5$ appear over longer and wider areas in the downstream direction behind a bubble.

5. Conclusions

In this study, a hybrid model for the constitutive law for non-Newtonian liquids which combines the Carreau model with the FENE-CR model was presented for computing the motion of a bubble rising through shear-thinning viscoelastic liquids. By hybridizing the Carreau model with the FENE-CR model, one can numerically replicate distinguishing features in both models. For example, for a large enough bubble (i.e. large enough *Eo*) one is able to reproduce a cusped cap bubble when ordinarily, without the non-Newtonian effects, one would have computed an oblate bubble instead. Simultaneously, the shear-thinning property induces a cap bubble shape from an oblate shape, and the viscoelastic property induces a cusp shape.

It is also demonstrated that one can analyze the relative effects of the shear-thinning property and of the viscoelastic property on the stress formed due to a rising gas bubble in a hybrid shear-thinning and viscoelastic liquid. Contour plots of $[c \times \mathrm{Tr}(\mathbf{A})]$ and $[\ \mathrm{Tr}(\mathbf{A})]$ enable one to more simply (rather than investigating all components of $\mathbf{A}$) isolate the viscoelastic and shear-thinning effects on a rising bubble.

Acknowledgments

This study was partially supported by the Grant-in-Aid for Scientific Research (C) (JP21560161) from the Japan Society for the Promotion of Science.

Supplementary material

Supplementary material associated with this article can be found, in the online version, at doi:10.1016/j.jnnfm.2018.12.012.

References

[1] P.J. Carreau, Rheological equations from molecular network theories, Trans. Soc. Rheol. 16 (1) (1972) 99–127, doi:10.1122/1.549276.
[2] M. Chilcott, J. Rallison, Creeping flow of dilute polymer solutions past cylinders and spheres, J. Non-Newton. Fluid Mech. 29 (1988) 381–432, doi:10.1016/0377-0257(88)85062-6.
[3] G. Astarita, G. Apuzzo, Motion of gas bubbles in non-Newtonian liquids, AlChE J. 11 (5) (1965) 815–820, doi:10.1002/aic.690110514.
[4] L.G. Leal, J. Skoog, A. Acrivos, On the motion of gas bubbles in a viscoelastic liquid, Can. J. Chem. Eng. 49 (5) (1971) 569–575, doi:10.1002/cjce.5450490504.
[5] A. Acharya, R. Mashelkar, J. Ulbrecht, Mechanics of bubble motion and deformation in non-Newtonian media, Chem. Eng. Sci. 32 (8) (1977) 863–872, doi:10.1016/0009-2509(77)80072-9.
[6] O. Hassager, Negative wake behind bubbles in non-Newtonian liquids, Nature 279 (1979) 402–403, doi:10.1038/279402a0.
[7] D. DeKée, P. Carreau, J. Mordarski, Bubble velocity and coalescence in viscoelastic liquids, Chem. Eng. Sci. 41 (9) (1986) 2273–2283, doi:10.1016/0009-2509(86)85078-3.
[8] D. De Kee, R.P. Chhabra, A photographic study of shapes of bubbles and coalescence in non-Newtonian polymer solutions, Rheol. Acta 27 (6) (1988) 656–660, doi:10.1007/BF01337462.
[9] Y.J. Liu, T.Y. Liao, D.D. Joseph, A two-dimensional cusp at the trailing edge of an air bubble rising in a viscoelastic liquid, J. Fluid Mech. 304 (1995) 321–342, doi:10.1017/S0022112095004447.
[10] D. Rodrigue, D.D. Kee, C.C.M. Fong, The slow motion of a single gas bubble in a non-Newtonian fluid containing surfactants, J. Non-Newton. Fluid Mech. 86 (1–2) (1999) 211–227, doi:10.1016/S0377-0257(98)00209-2.
[11] J. Herrera-Velarde, R. Zenit, D. Chehata, B. Mena, The flow of non-Newtonian fluids around bubbles and its connection to the jump discontinuity, J. Non-Newton. Fluid Mech. 111 (2–3) (2003) 199–209, doi:10.1016/S0377-0257(03)00055-7.
[12] R. Sousa, M. Riethmuller, A. Pinto, J. Campos, Flow around individual taylor bubbles rising in stagnant polyacrylamide (PAA) solutions, J. Non-Newton. Fluid Mech. 135 (1) (2006) 16–31, doi:10.1016/j.jnnfm.2005.12.007.
[13] C. Pilz, G. Brenn, On the critical bubble volume at the rise velocity jump discontinuity in viscoelastic liquids, J. Non-Newton. Fluid Mech. 145 (2–3) (2007) 124–138, doi:10.1016/j.jnnfm.2007.05.015.
[14] F. Wenyuan, M. Youguang, J. Shaokun, Y. Ke, L. Huaizhi, An experimental investigation for bubble rising in non-Newtonian fluids and empirical correlation of drag coefficient, J. Fluids Eng. 132 (2) (2010) 021305, doi:10.1115/1.4000739.
[15] S. Amirnia, J.R. de Bruyn, M.A. Bergougnou, A. Margaritis, Continuous rise velocity of air bubbles in non-Newtonian biopolymer solutions, Chem. Eng. Sci. 94 (2013) 60–68, doi:10.1016/j.ces.2013.02.032.
[16] M. Ohta, Y. Hieda, N. Tokui, S. Iwata, The motion of a bubble rising through viscoelastic polymeric liquids, Trans. JSME, (in Japanese) 81 (823) (2015) 14–00612, doi:10.1299/transjsme.14-00612.
[17] R. Zenit, J. Feng, Hydrodynamic interactions among bubbles, drops, and particles in non-Newtonian liquids, Annu. Rev. Fluid Mech. 50 (1) (2018) 505–534, doi:10.1146/annurev-fluid-122316-045114.
[18] D.S. Noh, I.S. Kang, L.G. Leal, Numerical solutions for the deformation of a bubble rising in dilute polymeric fluids, Phys. Fluids A 5 (6) (1993) 1315–1332, doi:10.1063/1.858568.
[19] A. Wagner, L. Giraud, C. Scott, Simulation of a cusped bubble rising in a viscoelastic fluid with a new numerical method, Comput. Phys. Commun. 129 (1–3) (2000) 227–232, doi:10.1016/S0010-4655(00)00109-0.
[20] S. Pillapakkam, P. Singh, A level-set method for computing solutions to viscoelastic two-phase flow, J. Comput. Phys. 174 (2) (2001) 552–578, doi:10.1006/jcph.2001.6927.
[21] X. Frank, H.Z. Li, Complex flow around a bubble rising in a non-Newtonian fluid, Phys. Rev. E 71 (3) (2005) 036309, doi:10.1103/PhysRevE.71.036309.
[22] C. Málaga, J. Rallison, A rising bubble in a polymer solution, J. Non-Newton. Fluid Mech. 141 (1) (2007) 59–78, doi:10.1016/j.jnnfm.2006.07.012.
[23] S.B. Pillapakkam, P. Singh, D. Blackmore, N. Aubry, Transient and steady state of a rising bubble in a viscoelastic fluid, J. Fluid Mech. 589 (2007) 215–252, doi:10.1017/S0022112007007628.
[24] M. Ohta, K. Onodera, Y. Yoshida, M. Sussman, Three-dimensional numerical simulations of a rising bubble in a viscoelastic fenecr model fluid, AIP Conf. Proc. 1027 (1) (2008) 896–898, doi:10.1063/1.2964886.
[25] R. You, A. Borhan, H. Haj-Hariri, Stability analysis of cusped bubbles in viscoelastic flows, J. Fluid Mech. 621 (2009) 131–154, doi:10.1017/S0022112008004795.
[26] S. Lind, T. Phillips, The effect of viscoelasticity on a rising gas bubble, J. Non-Newton. Fluid Mech. 165 (15–16) (2010) 852–865, doi:10.1016/j.jnnfm.2010.04.002.
[27] D. Fraggedakis, M. Pavlidis, Y. Dimakopoulos, J. Tsamopoulos, On the velocity discontinuity at a critical volume of a bubble rising in a viscoelastic fluid, J. Fluid Mech. 789 (2016) 310–346, doi:10.1017/jfm.2015.740.
[28] M. Pang, M. Lu, Numerical study on dynamics of single bubble rising in shear-thinning power-law fluid in different gravity environment, Vacuum 153 (2018) 101–111, doi:10.1016/j.vacuum.2018.04.011.
[29] R. You, A. Borhan, H. Haj-Hariri, A finite volume formulation for simulating drop motion in a viscoelastic two-phase system, J. Non-Newton. Fluid Mech. 153 (2–3) (2008) 109–129, doi:10.1016/j.jnnfm.2007.12.002.
[30] M. Ohta, K. Onodera, Y. Yoshida, M. Sussman, Three-dimensional simulations of the dynamic motion of single drops rising in viscoelastic FENE-CR model fluids, J. Chem. Eng. Jpn. 42 (10) (2009) 705–712, doi:10.1252/jcej.09we031.
[31] M. Ohta, E. Iwasaki, E. Obata, Y. Yoshida, A numerical study of the motion of a spherical drop rising in shear-thinning fluid systems, J. Non-Newton. Fluid Mech. 116 (1) (2003) 95–111, doi:10.1016/j.jnnfm.2003.08.004.
[32] M. Ohta, E. Iwasaki, E. Obata, Y. Yoshida, Dynamic processes in a deformed drop rising through shear-thinning fluids, J. Non-Newton. Fluid Mech. 132 (1) (2005) 100–107, doi:10.1016/j.jnnfm.2005.10.008.
[33] J. Tsamopoulos, Y. Dimakopoulos, N. Chatzidai, G. Karapetsas, M. Pavlidis, Steady bubble rise and deformation in Newtonian and viscoplastic fluids and conditions for bubble entrapment, J. Fluid Mech. 601 (2008) 123–164, doi:10.1017/S0022112008000517.

[34] M. Ohta, Y. Yoshida, M. Sussman, A computational study of the dynamic motion of a bubble rising in Carreau model fluids, Fluid Dyn. Res. 42 (2) (2010) 025501, doi:10.1088/0169-5983/42/2/025501.
[35] L. Zhang, C. Yang, Z.-S. Mao, Numerical simulation of a bubble rising in shear-thinning fluids, J. Non-Newton. Fluid Mech. 165 (11) (2010) 555–567, doi:10.1016/j.jnnfm.2010.02.012.
[36] M. Ohta, S. Kimura, T. Furukawa, Y. Yoshida, M. Sussman, Dynamics of an air bubble rising in a non-Newtonian liquid in the axisymmetric regime, J. Chem. Eng. Jpn. 45 (9) (2012) 713–720, doi:10.1252/jcej.12we041.
[37] Y. Dimakopoulos, M. Pavlidis, J. Tsamopoulos, Steady bubble rise in Herschel–Bulkley fluids and comparison of predictions via the augmented lagrangian method with those via the papanastasiou model, J. Non-Newton. Fluid Mech. 200 (2013) 34–51, doi:10.1016/j.jnnfm.2012.10.012.
[38] M.K. Tripathi, K.C. Sahu, G. Karapetsas, O.K. Matar, Bubble rise dynamics in a viscoplastic material, J. Non-Newton. Fluid Mech. 222 (2015) 217–226, doi:10.1016/j.jnnfm.2014.12.003.
[39] A. Premlata, M.K. Tripathi, B. Karri, K.C. Sahu, Dynamics of an air bubble rising in a non-Newtonian liquid in the axisymmetric regime, J. Non-Newton. Fluid Mech. 239 (2017) 53–61, doi:10.1016/j.jnnfm.2016.12.003.
[40] A.R. Premlata, M.K. Tripathi, B. Karri, K.C. Sahu, Numerical and experimental investigations of an air bubble rising in a Carreau–Yasuda shear-thinning liquid, Phys. Fluids 29 (3) (2017) 033103, doi:10.1063/1.4979136.
[41] J.G. Oldroyd, On the formulation of rheological equations of state, Proc. R. Soc. Lond. A: Math. Phys. Eng. Sci. 200 (1063) (1950) 523–541, doi:10.1098/rspa.1950.0035.
[42] D. Boger, A highly elastic constant-viscosity fluid, J. Non-Newton. Fluid Mech. 3 (1) (1977) 87–91, doi:10.1016/0377-0257(77)80014-1.
[43] N. Phan-Thien, R.I. Tanner, A new constitutive equation derived from network theory, J. Non-Newton. Fluid Mech. 2 (4) (1977) 353–365, doi:10.1016/0377-0257(77)80021-9.
[44] R. Bird, P. Dotson, N. Johnson, Polymer solution rheology based on a finitely extensible bead—spring chain model, J. Non-Newton. Fluid Mech. 7 (2) (1980) 213–235, doi:10.1016/0377-0257(80)85007-5.
[45] M. Herrchen, H.C. Öttinger, A detailed comparison of various fene dumbbell models, J. Non-Newton. Fluid Mech. 68 (1) (1997) 17–42, doi:10.1016/S0377-0257(96)01498-X.
[46] H. Giesekus, A simple constitutive equation for polymer fluids based on the concept of deformation-dependent tensorial mobility, J. Non-Newton. Fluid Mech. 11 (1) (1982) 69–109, doi:10.1016/0377-0257(82)85016-7.
[47] K. Yasuda, R.C. Armstrong, R.E. Cohen, Shear flow properties of concentrated solutions of linear and star branched polystyrenes, Rheol. Acta 20 (2) (1981) 163–178, doi:10.1007/BF01513059.
[48] F. Pimenta, M. Alves, Stabilization of an open-source finite-volume solver for viscoelastic fluid flows, J. Non-Newton. Fluid Mech. 239 (2017) 85–104, doi:10.1016/j.jnnfm.2016.12.002.
[49] M. Ohta, M. Sussman, The buoyancy-driven motion of a single skirted bubble or drop rising through a viscous liquid, Phys. Fluids 24 (11) (2012) 112101, doi:10.1063/1.4765669.
[50] P.A. Stewart, N. Lay, M. Sussman, M. Ohta, An improved sharp interface method for viscoelastic and viscous two-phase flows, J. Sci. Comput. 35 (1) (2008) 43–61, doi:10.1007/s10915-007-9173-5.
[51] M. Sussman, E.G. Puckett, A coupled level set and volume-of-fluid method for computing 3d and axisymmetric incompressible two-phase flows, J. Comput. Phys. 162 (2) (2000) 301–337, doi:10.1006/jcph.2000.6537.
[52] M. Sussman, K. Smith, M. Hussaini, M. Ohta, R. Zhi-Wei, A sharp interface method for incompressible two-phase flows, J. Comput. Phys. 221 (2) (2007) 469–505, doi:10.1016/j.jcp.2006.06.020.
[53] C. Hirt, B. Nichols, Volume of fluid (vof) method for the dynamics of free boundaries, J. Comput. Phys. 39 (1) (1981) 201–225, doi:10.1016/0021-9991(81)90145-5.
[54] J.E. Pilliod Jr, E.G. Puckett, Second-order accurate volume-of-fluid algorithms for tracking material interfaces, J. Comput. Phys. 199 (2) (2004) 465–502, doi:10.1016/j.jcp.2003.12.023.
[55] M. Sussman, P. Smereka, S. Osher, A level set approach for computing solutions to incompressible two-phase flow, J. Comput. Phys. 114 (1) (1994) 146–159, doi:10.1006/jcph.1994.1155.
[56] M. Sussman, A.S. Almgren, J.B. Bell, P. Colella, L.H. Howell, M.L. Welcome, An adaptive level set approach for incompressible two-phase flows, J. Comput. Phys. 148 (1) (1999) 81–124, doi:10.1006/jcph.1998.6106.
[57] M. Ohta, T. Imura, Y. Yoshida, M. Sussman, A computational study of the effect of initial bubble conditions on the motion of a gas bubble rising in viscous liquids, Int. J. Multiphase Flow 31 (2) (2005) 223–237, doi:10.1016/j.ijmultiphaseflow.2004.12.001.